remote sensing

MDPI

Article

Mapping Young Lava Rises (Stony Rises) Across an Entire Basalt Flow Using Remote Sensing and Machine Learning

Shaye Fraser [1,*], Mariela Soto-Berelov [1], Lucas Holden [1], John Webb [2] and Simon Jones [1]

[1] School of Science, RMIT University, Melbourne, VIC 3000, Australia; mariela.soto-berelov@rmit.edu.au (M.S.-B.); lucas.holden@rmit.edu.au (L.H.); simon.jones@rmit.edu.au (S.J.)
[2] Department of Ecology, Plant and Soil Science, La Trobe University, Melbourne, VIC 3086, Australia; john.webb@latrobe.edu.au
* Correspondence: s3661928@student.rmit.edu.au

Abstract: Lava rises, locally known as stony rises, are Pliocene–Holocene volcanic landforms occurring throughout the Victorian Volcanic Plain (VVP) in Victoria, Australia. Stony rises are not only important to understanding the geological history of Victoria but are culturally significant to Aboriginal Australians and have ecological importance. Currently, the mapping of stony rises is manually performed at a case study level rather than a landscape level. Remote sensing technologies such as LiDAR data, satellite imagery, and aerial imagery allow for the mapping of stony rises from an aerial perspective. This paper aims to map stony rises using remotely sensed and geophysical data at a landscape level on a younger lava flow (~42,000 years old) within the Victorian Volcanic Plain (the Warrion Hill and Red Rock Volcanic Complex) by utilizing an object based random forest machine learning approach. The results show that stony rises were successfully identified in the landscape to an accuracy of 78.9%, with 2716 potential new stony rises identified. Out of 34 predictor variables, we found the most important variables to be slope gradient, local elevation, DEM of Difference (change in height), Normalized Difference Water Index (NDWI), Clay Mineral Ratio, the concentration of radiometric elements (Potassium, Thorium, and Uranium), Total Magnetic Intensity, and Ecological Vegetation Class (EVC). The results from this study highlight the ability to detect a volcanic landform at a landscape scale using an ensemble of predictor variables that include topographic, spectral information and geophysical data. This lays the foundation towards a uniform approach for mapping stony rises throughout the VVP and similar landforms (such as tumuli) worldwide.

Keywords: stony rises; lava rises; object based random forest; remote sensing; machine learning

check for updates

Academic Editor: Annalisa Cappello

Received: 6 May 2025
Revised: 30 May 2025
Accepted: 3 June 2025
Published: 10 June 2025

Citation: Fraser, S.; Soto-Berelov, M.; Holden, L.; Webb, J.; Jones, S. Mapping Young Lava Rises (Stony Rises) Across an Entire Basalt Flow Using Remote Sensing and Machine Learning. *Remote Sens.* **2025**, *17*, 2004. https://doi.org/10.3390/rs17122004

Copyright: © 2025 by the authors. Licensee MDPI, Basel, Switzerland. This article is an open access article distributed under the terms and conditions of the Creative Commons Attribution (CC BY) license (https://creativecommons.org/licenses/by/4.0/).

1. Introduction

The Victorian Volcanic Plain (VVP) in southeastern Australia extends westwards from metropolitan Melbourne for ~410 km, covering an area of ~19,000 km^2, and contains nearly 700 eruption points [1], including many complex volcanic centers, such as the Red Rock volcanic complex (Figure 1). Many of the basalt lava flows of the VVP have hummocky surfaces, with prominent elevated areas locally known as stony rises. Stony rises are equivalent to lava rises and tumuli [2] which can be found on lava flows in Hawaii [3] and the Snake River Plains in Idaho [4].

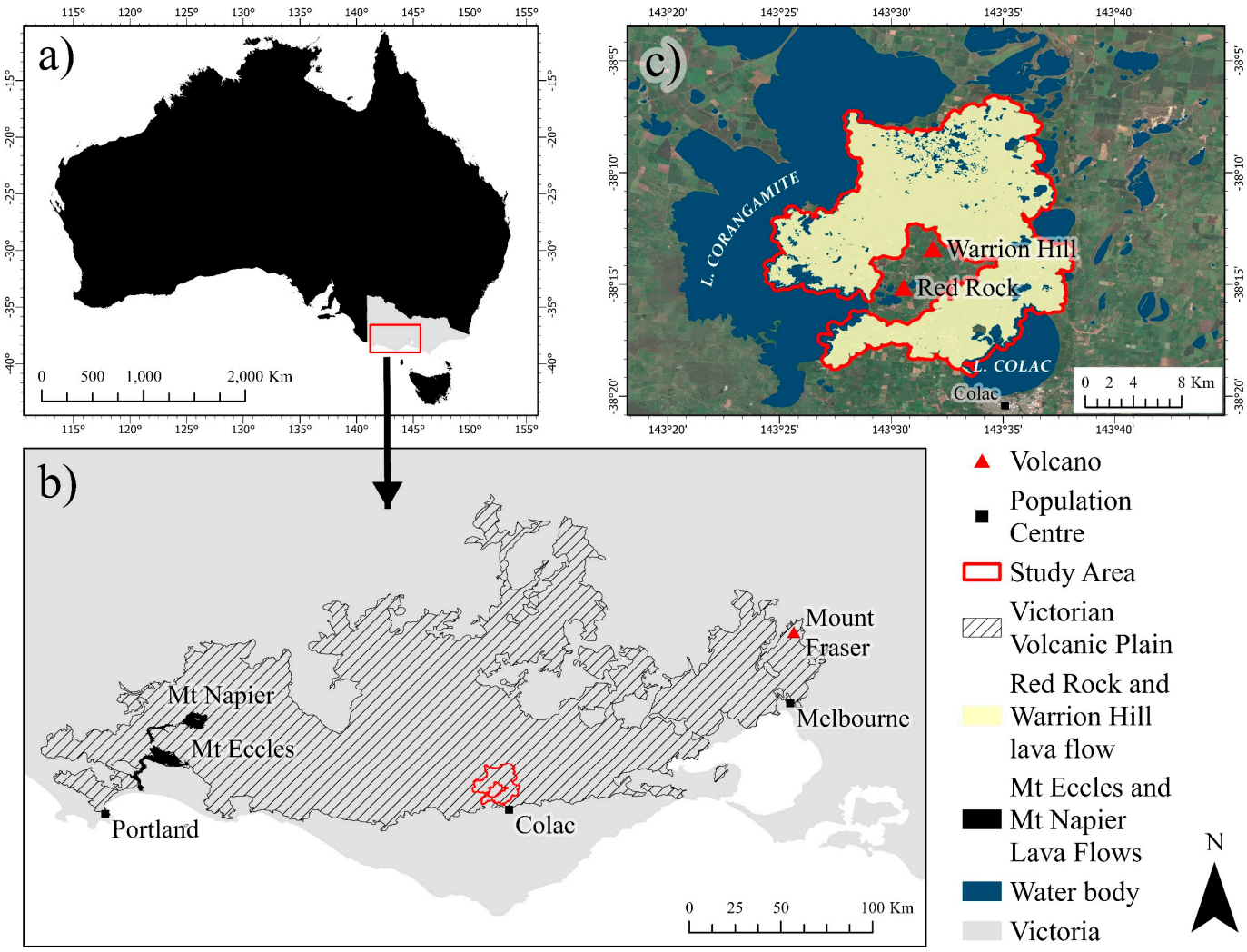


Figure 1. (**a**) The location of the Victorian Volcanic Plain (VVP) in Australia, (**b**) the study area and other volcanoes' locations in the VVP, (**c**) the study area (red polygon) in relation to the Warrion Hill and Red Rock volcanoes.

The basalt volcanoes that created the stony rises erupted between ~8 million years ago [5] to as recent as ~5000 years ago [6], and the VVP can be classified as an active lava field, with eruptions likely to occur in the future [7]. Each individual lava flow is typically 1–2 m thick, building up over time to create a thickness of up to 120 m [7]. On lava flows older than a million years, stony rises have largely weathered away, so the surfaces of the flows are flat and covered in clay-rich soils [8,9]. Stony rises on lava flows younger than a million years are more prominent, typically rising 5–8 m above the surrounding landscape [10]. Stony rises on the Mt Fraser lava flow (~800,00 years old) [5,11], close to Melbourne on the eastern edge of the VVP, take the form of round or elliptical mounds (typically a few meters across) or larger flat-top plateaus that can be hundreds of meters across [8]. Stony rises on some of the youngest lava flows in the VVP such as Mt Eccles (~36,900 years old) [12], Mt Napier (~48,500 years old), and Red Rock (~42,000 years old) are very well-preserved [13] (Figure 2). They have had little modification from weathering and are easily visible on aerial and satellite imagery. They can rise up to 10 m high [14] and are covered in boulders, native vegetation, and thin red-brown loam soils [8].



Figure 2. A selection of stony rises from the Warrion Hill and Red Rock lava flows: (**a**) a large stony rise with cattle grazing on its slopes; (**b**) a collection of stony rises covered in large, exposed basalt boulders with a drystone wall following the ridgelines; (**c**) a stony rise covered in vegetation.

Stony rises are considered to have high geological, ecological, and cultural value. Geologically, stony rises represent part of the rich volcanic history of the VVP [15]. Ecologically, the VVP hosts many native flora and fauna species [10,16]. Culturally, Aboriginal artefact deposits are often found on stony rises and provide evidence of Aboriginal land use of the volcanic landscape [17]. Stony rises were also used as a resource by European settlers, who utilized the basalt in the construction of drystone walls and farm buildings [10]. Additionally, stony rises from the Mt Eccles lava flows (Figure 1) contributed to the Aboriginal eel traps and aquaculture system found within the UNESCO World Heritage Site of Budj Bim [10]. Given the significance of stony rises, there are efforts in advocating for their protection beyond the UNESCO World Heritage Site. However, they need to be mapped first to do this effectively.

Currently, stony rises in the VPP are mapped on a case-by-case basis by conducting traditional field surveys [17–22]. These field surveys can have low mapping accuracy due to vegetation obscuring the ground surface and irregular terrain, making it a potentially dangerous on-ground activity [18,22]. This has resulted in many stony rises within the VVP remaining under-mapped or unmapped, such as the ones from the Red Rock and Warrion Hill lava flows. This may be due to limited resources from local municipalities, geologists, cultural practitioners, and ecologists, as well as limited accessibility because

they often occur on private property. With the availability of newer remotely sensed data with high spatial resolution (~1 m cell spacing) and large coverage over parts of the VVP, there now exists an opportunity to map stony rises with geophysical data, LiDAR data, and satellite and aerial imagery at a broader scale. When working with such datasets (with high spatial resolution) at a landscape level, machine learning has been shown to offer a suitable environment for landform detection [23].

Fraser et al. [8] used remotely sensed and geophysical data, combining Object Based Image Analysis (OBIA) [24–30] and Random Forest (RF) [31–35] techniques, to successfully map stony rises from the Mt Fraser lava flow in metropolitan Melbourne, Australia. This approach has been used successfully (>90% accuracy) in vegetation studies [36,37], agricultural studies [38–41], settlement identification [42], and land use land cover classification [43] worldwide and has been shown to significantly outperform existing techniques [44,45]. OBIA implements an image segmentation algorithm which creates image segments (also known as image objects) based on spectral homogeneity [26] and allows for contextual information such as shape and size to be considered through the classification process [29]. RF is a classification technique that uses decision trees and is reliant on a variety of predictor variables, which are used to train machine learning [46,47]. More information about each technique can be accessed in the References [26,46].

Their success requires the availability of sufficient predictor variables (for RF) and representative geometric attributes (shape and size for OBIA) for training the machine learning model. In study areas where significant data exist and the spatial attributes of the features are well characterized, the machine learning model performs well (as seen in Fraser et al. [8]). However, in areas where this data is not available, significant challenges exist. A machine learning model used successfully at one study site may not necessarily work at another site in a different location or size.

This research applies the technique utilized by Fraser et al. [8] to map stony rises at a landscape scale across the Warrion Hill and Red Rock Volcanic Complex lava flows (see Figure 1c) in the vicinity of Colac, Australia. This is the first time that machine learning using remotely sensing data has been applied to map stony rises in this area and the first time the approach has been used to map an entire lava flow. This is a significantly larger study area than the previously mapped Mount Fraser lava flow [8] and contains numerous younger (~42,000 years old) well preserved stony rises, with different physical characteristics. The remote sensing data available across this study area is not temporally coincident with that used in Fraser et al. [8]. The results will provide important information about the distribution and nature of stony rises in this vicinity as well as offer insights into the transferability and scalability of machine learning utilizing remote sensing to map stony rises across different natural landscapes.

2. Study Area

The ~565 km^2 study area is located in rural Victoria, Australia, approximately 140 km southwest of Melbourne CBD (Figure 2). The study area sits within the Corangamite drainage basin and comprises the stony rise basalt lavas that erupted from the Warrion Hill and Red Rock Volcanic Complex (with an additional 250 m buffer surrounding the lava flows). Lake Corangamite marks the western boundary of the lava flows, while a series of smaller volcanic lakes lie along the eastern boundary.

The climate of the Corangamite Basin has warm and dry summers and cool and wet winters [16], with an average annual rainfall of approximately 720 mm [48]. The native vegetation of the study area and its surrounds (Figure 3) comprises 12 vegetation classes dominated by Stony Rises Woodlands and Plains Grassy Woodlands.

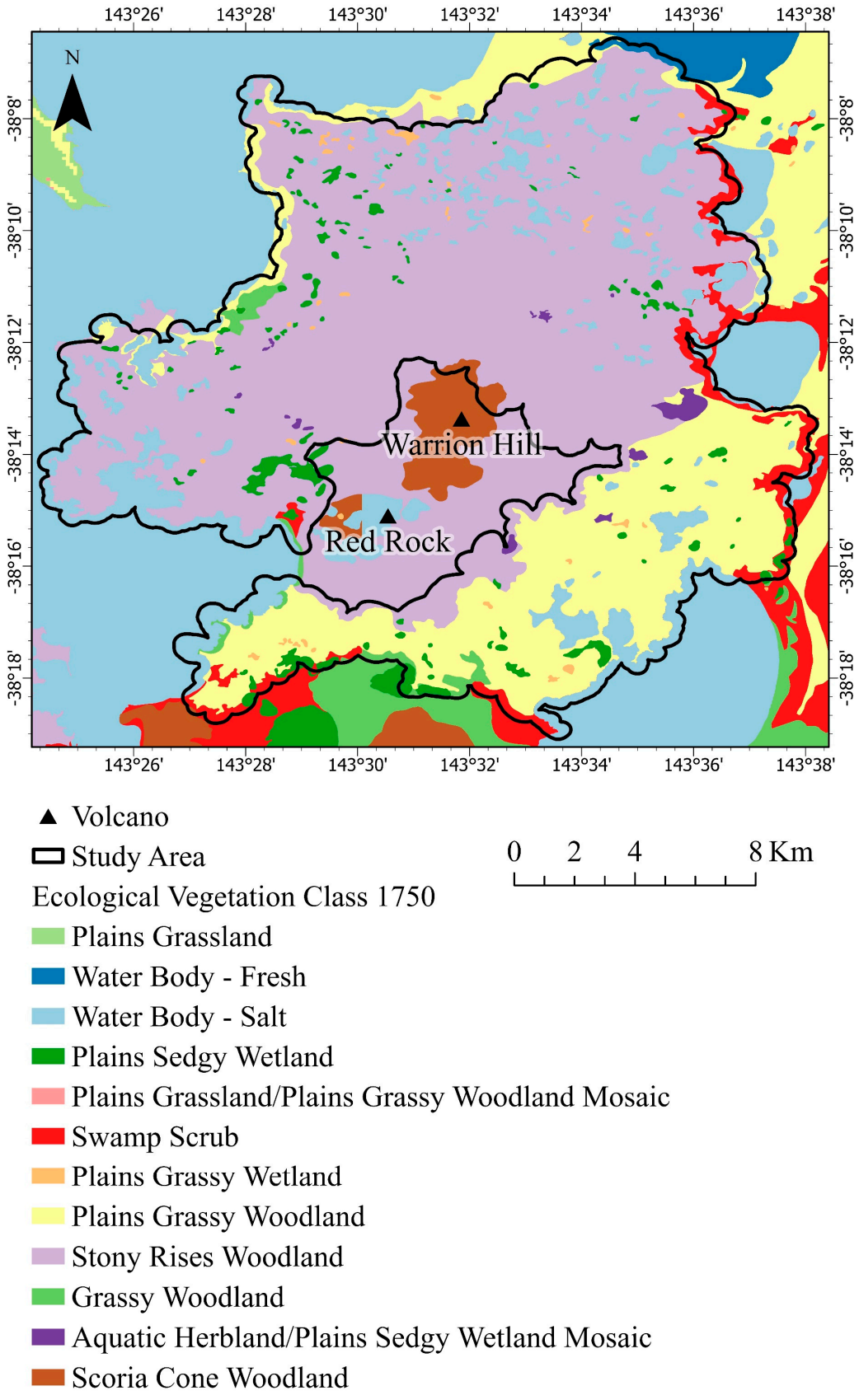


Figure 3. Ecological Vegetation Classes (EVCs) (mapped 1750) within the study area. The two prominent EVCs are Stony Rises Woodland as seen dominating the northern part of the study area, and Plains Grassy Woodland dominating the southern part of the study area.

The earliest volcanic activity from Warrion Hill and the Red Rock Volcanic Complex comprised effusive pahoehoe lava flows, probably from Warrion Hill [49]. This eruption was followed by relatively minor pahoehoe lava flows from an unknown vent at the Red Rock maar-scoria cone complex, which lies ~5 km southwest of Warrion Hill. Then extensive magmatic and phreatomagmatic eruptions from numerous vents at Red Rock covered the lava flows near the vents with thick volcanic ash deposits. Oostingh et al. [13] dated one of the Warrion Hill/Red Rock cones as approximately 42,000 years old, making the volcanic activity at this site among the youngest within the VVP.

The ash deposits surrounding the Warrion Hill/Red Rock volcanoes have obscured the lava flow surface features, including stony rises; as a result the area covered by ash was excluded from this study (Figure 3). It is notable that the ash deposits have thicker soils than the lava flows and are extensively cropped, whereas land use on the basalt lavas is restricted to grazing.

To the north of the volcanoes, two separate lava flows, both probably from Warrion Hill, are evident: an older flow with well-developed stony rises overlain by a younger flow with a much smoother surface. The boundary of the younger flow is a cliff-line up to 10 m high in places but becomes less defined to the west. The lack of stony rises on the younger flow may be due to a faster lava-supply rate, as shown by observations of flowing lava on Hawaii [50]. In other parts of the VVP, the lack of stony rises is largely related to the age of the flows; on lavas older than 1 million years, stony rises have generally weathered away [8].

3. Materials and Methods

3.1. Data

The data used in this study was obtained from open-source repositories (see Table 1) and selected as they help describe the spatial characteristics of stony rises as defined in Fraser et al. [8,51]. LiDAR data collected between 2006 and 2007 [52] was used to derive the topographic variables (aspect, change in height (DEM of Difference), local elevation, slope gradient, and surface terrain roughness). Before the topographic variables were derived, the LiDAR data was filtered for ground points to remove the noise of vegetation, buildings, powerlines, etc. The LiDAR data had a density of 2 points per meter which is acceptable to map individual stony rise landforms [8].

Satellite imagery from Sentinel-2 [53] was used to derive spectral information such as indices and ratios. This study used the Normalized Difference Water Index (NDWI) developed by [54], the Clay Mineral Ratio, and the Iron Oxide Ratio (see formulas below).

$$\text{NDWI} = (\text{NIR} - \text{SWIR})/(\text{NIR} + \text{SWIR}), \quad (1)$$

$$\text{Iron Oxide Ratio} = \text{Red}/\text{Blue}, \quad (2)$$

$$\text{Clay Mineral Ratio} = \text{SWIR1}/\text{SWIR2} \quad (3)$$

The bands are described as NIR (0.79–0.90 μm near-infrared band), SWIR1 (1.57–1.66 μm the short-wave infrared band), SWIR2 (2.11–2.28 μm short-wave infrared band), Red (0.65–0.88 μm), and Blue (0.49–0.52 μm) [55].

As stony rises are generally drier than the surrounding grasslands [21,51], the NDWI was used to detect the moisture content throughout the landscape. atellite imagery captured between the months of July and November (inclusive) is ideal for detecting stony rises with the NDWI in the VVP due to the high contrast in the moisture between stony rises and the surrounding grasslands [51]. The Clay Mineral Ratio and Iron Oxide Ratio were used to

derive geological spectral information. Imagery collected on November 1, 2021, was used as this provided a cloud-free image across the study area.

Aerial imagery (red, green, and blue reflectance) captured as part of the *2018–2019 South West Rural Photography* campaign at a spatial resolution of 0.15 m per pixel [56] was used for contextual information and the image segmentation. The red, green, and blue reflectance was also used for additional spectral information and as potential predictor variables for the RF algorithm.

Airborne geophysical data [57] utilized in this study includes airborne radiometrics (used to derive the concentration of Potassium (K), Thorium (Th), and Uranium (U) metrics) and geomagnetics (used to derive the Total Magnetic Intensity (TMI) and the first vertical derivative). The grid cell resolution of the geophysical data is 50 m across the state of Victoria (including the study area). While the grid cell resolution is too coarse to measure individual stony rise landforms, it can help delineate the boundaries of different geomagnetic features and geological landform units such as lava flows [57].

Non-remotely sensed datasets used in this study included native Ecological Vegetation Class (EVC) information [58]. EVCs help to provide contextual information of the landscape as well as being a characteristic of stony rises [51].

Unlike Fraser et al. [8] who had LiDAR data and aerial imagery captured within a year of each other, the LiDAR and aerial imagery used in this study has been collected infrequently. However, this study area is located in rural Australia, with the main land cover type being agriculture and minimal landcover change has occurred in the study area between the LiDAR capture date (2008) and the aerial imagery (2019).

3.2. Method

The overview of the methodology is shown in Figure 4. Following a similar approach to Fraser et al. [8], the methodology is broken down into the creation of training data, preparation of input predictor variables, image segmentation, and training and classification of stony rises using a Random Forest classifier. The details of each of these steps are briefly described in the following sections.

3.2.1. Preparation of Training Data

In order for the machine learning algorithm to appropriately learn the stony rise characteristics, training data that represents the range of shapes and sizes of the landform of interest is needed [59]. To our knowledge, there has been no mapping of stony rises across the Warrion Hill and Red Rock lava flows. A bespoke training dataset of stony rises was created by the authors using field observation, Google Street View, and aerial imagery draped over a LiDAR-derived hillshade and slope map. The identified stony rises were manually digitized as polygons in ArcGIS Pro (Version 3.0.3). This manual interpretation resulted in 890 stony rises being digitized within the study area, comprising of large, small, simple, and more complex stony rise landforms. To ensure the quality of the training dataset, an expert geomorphologist was consulted to assure there was a good cross section of the stony rises present within the study area. The observed minimum stony rise size is 104 m^2 and the maximum observed size is 1,536,032 m^2. The stony rises have slopes ranging from 0° (as seen on the flat ridgelines) to as steep as 56°.

Table 1. Remotely sensed and geophysical datasets used in this study to derive the input predictor variables for the Random Forest algorithm. Information such as the spatial resolution, central wavelength of bands, sensor information, date of capture, and data source are detailed.

	Spatial Resolution	Bands (Central Wavelength)	Sensor	Date of Data Capture	Date/Source
Aerial imagery	0.15 m per pixel	Red, Green, Blue	VisionMap A3—Edge	28 January 2019–17 May 2019	2018–19 South West Rural Photography [56]
Sentinel-2 Satellite imagery	Bands 2–4, 8: 10 m per pixel; Bands 5–7, 8A, 11, 12: 20 m per pixel	Band 2 (blue): 0.490 µm Band 3 (green): 0.560 µm Band 4 (red): 0.665 µm Band 5 (Vegetation Red Edge): 0.705 µm Band 6 (Vegetation Red Edge): 0.740 µm Band 7 (Vegetation Red Edge): 0.783 µm Band 8 (Near Infrared): 0.842 µm Band 8A (Vegetation Red Edge): 0.865 µm Band 11 (Shortwave Infrared): 1.610 µm Band 12 (Shortwave Infrared): 2.190 µm	Sentinel-2A	1 November 2021	S2B_MSIL2A_20211101T002059_N0301_R116_T54HYC_20211101T021017.SAFE [56]
LiDAR	2 points per meter	N/A	ALTM Gemini, Optech ALTM Orion	14 January 2008–23 March 2008	2006-07 South-West Region LiDAR—Corangamite [52]
Airborne radiometric and aeromagnetic	50 m; 200–400 m across metropolitan Melbourne, Victoria	Potassium: counts per second or % Thorium: counts per second or ppm Uranium: counts per second or ppm Total Magnetic Intensity: nT First Magnetic Derivative nT/m	Various Flight lines 110–10,000 m	Various between 1956 and 2001	Victoria Airborne and Gravity 2008 [57]

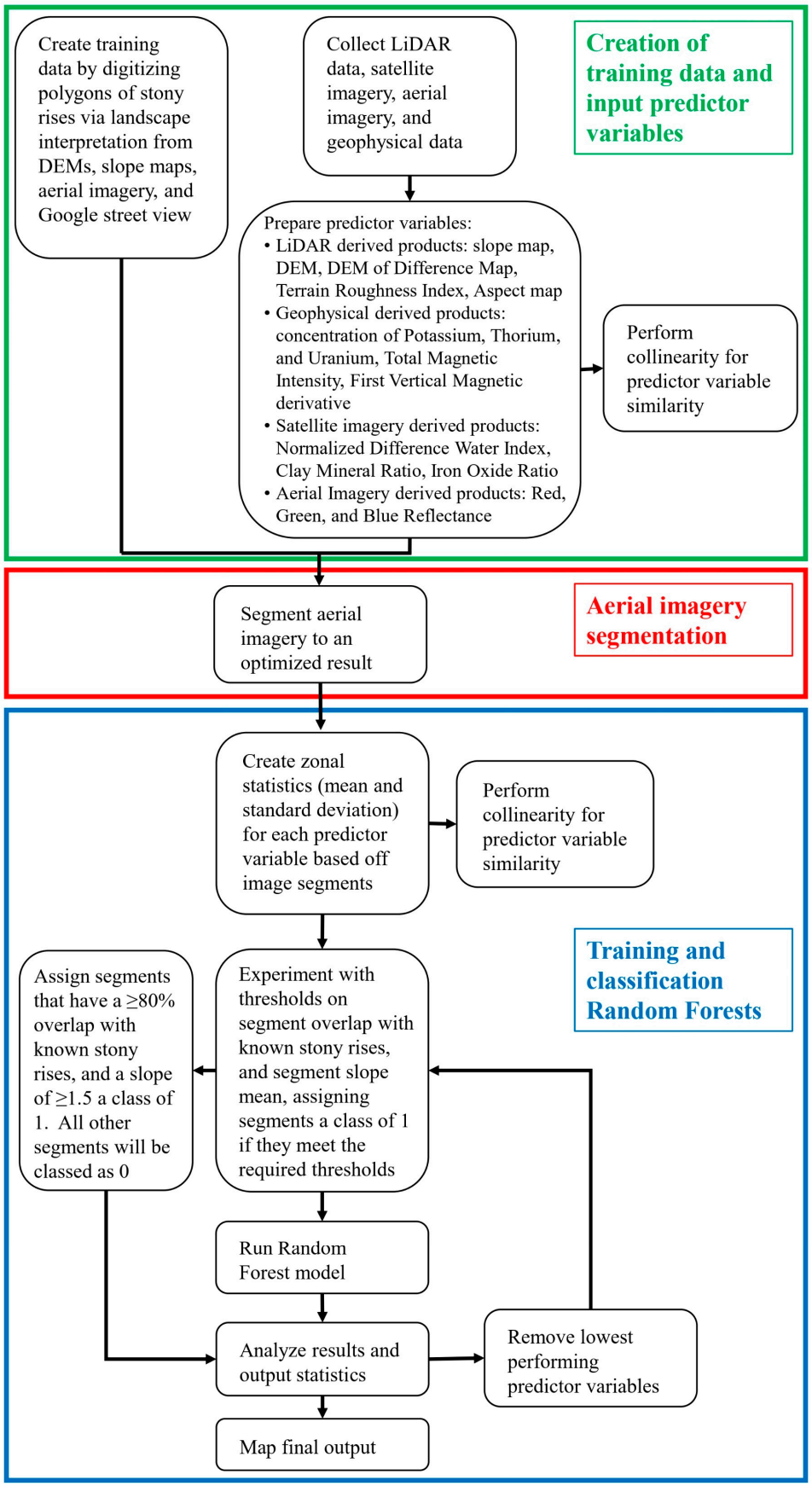


Figure 4. Workflow of the methodology followed to detect stony rise landforms in the Warrion Hill and Red Rock lava flow. It consists of (1) the preparation of training data, (2) image segmentation, and (3) the training and classification of the Random Forest Model.

3.2.2. Preparation of Input Predictor Variables

Based on the dimensions of the observed stony rises and the spatial resolution of the various datasets collected (Table 1), it was deemed that all the input predictor variables should have a spatial resolution of 1 m. This was chosen as the LiDAR data used was appropriate for mapping at a resolution of 1 m and helped to reduce the data processing time. Additionally, this would also ensure that smaller stony rises could still be detected. All the satellite-derived variables (NDWI, Clay Mineral Ratio, and Iron Oxide Ratio), geophysical-derived variables (concentration of K, Th, U, and TMI and the magnetic first vertical derivative), and the aerial imagery were resampled using bilinear interpolation to 1 m. Collinearity, using Pearsons's correlation coefficient, was then performed for the input predictor variables, to identify variables with potential high correlation.

3.2.3. Image Segmentation

Using the Orfeo Toolbox (OTB), plugin in QGIS, OBIA segmentation was performed. The OTB was developed by the French Space Agency for the purpose of analyzing remotely sensed imagery [60]. The segmentation was performed on the 2019 aerial imagery using a multi-threaded Mean-Shift algorithm (see [61] for more information). The minimum mapping unit was defined as 100 pixels due to the smallest digitized stony rise having a size of 104 m^2 (or 104 pixels). It is recommended to make the minimum mapping unit smaller than the smallest known object [62]. A total of 819,085 image objects were produced by the OBIA segmentation. The segmentation results were visually inspected to ensure that the digitized stony rises had adequate segmentation.

3.2.4. Training and Classifying Using a Random Forest Classifier

The zonal statistics of mean and standard deviation were calculated for the image objects. This was performed on all of the raster datasets (LiDAR-derived DEM derivatives, spectral indices and ratios, and geophysical data). Due to the EVC data being categorical, the majority class for each image object was computed. Collinearity, using Pearsons's correlation coefficient, was performed again for any potential variable bias between the input predictor variables when running the RF classification.

In this study, a number of thresholds were used to help define and classify the stony rise landforms. These include the minimum mapping unit (100 pixels), the segment purity ($\geq$80% of an image object falls within a known stony rise), and a slope gradient of ($\geq$1.5°). These thresholds are based on initial assumptions that the geometry of the stony rises in the study area are less weathered and still resemble their initial structure from ~42,000 years ago (e.g., 80% purity) and are locally prominent (e.g., a higher elevation than the surrounding landscape) with clearly defined slopes. The impact of these thresholds and the assumption they are based on is discussed in more detail later, particularly in comparison to the earlier study of Fraser et al. [8]. A binary classification of stony rises was also used, with a class of 1 representing presence and a class of 0 representing absence. This resulted in 40,028 segments (~4.9% of segments) being classified as 1 (stony rise present) and ~95.1% of segments being classified as 0 (stony rise absence).

Rstudio (and its packages *carat* [63] and *randomForest* [64]) was used to create and run the RF algorithm. Here, 200,000 segments identified as non-stony rises and 20,000 training image segments identified as stony rises were randomly selected to train the RF. Of the randomly selected data, 70% of the segments were used to train the RF model, with the remaining 30% used for validation.

Once the RF model was trained, the algorithm was then applied to the whole dataset. All 34 potential input predictor variables shown in Table 2 (detailed in [8,51]) were implemented in the RF model on its first iteration. Then, the table of Relative Variable of

Importance was examined throughout each iteration and was compared to the collinearity results. Using the Mean Decrease Gini value as an indicator, the variables of least importance were slowly eliminated in subsequent iterations to produce the top performing variables. Additionally, the RF model was optimized by altering the number of decision trees and the number of variables randomly selected at each decision split. It became apparent within the first few iterations of the RF classification that more refinement regarding the selection of input variables, and thresholds such as segment purity and slope gradient, needed to be experimented with to produce optimal results. This is discussed in greater detail in the Discussion section.

For this study we use the definition of stony rise detection stated by Fraser et al. [8]. A stony rise was deemed detected if one or more segments within the known stony rise polygon were detected. Therefore, a newly detected stony rise is defined as one or more segments clustered together that are not touching or directly adjacent to a known stony rise polygon.

Table 2. All the predictor variables considered for this study and inputted into the initial Random Forest classification. The predictor variables in bold and with an asterisk (*) are the input predictor variables used in the final model run and results. The predictor variables with (ˆ) were used in Fraser et al. [8] when mapping older stony rises but were not required in this study.

Variable Cohort			
Topography	**Spectral Signature and Indices**	**Airborne Geophysics**	**Vegetation**
Aspect Mean	**Normalized Difference Water Index Mean *ˆ**	**Concentration of Potassium Mean ***	
Aspect Std Dev	Normalized Difference Water Index Std Dev	Concentration of Potassium Std Dev	
DEM of Difference Mean *	Iron Oxide Ratio Mean	**Concentration of Thorium Mean *ˆ**	
DEM of Difference Std Dev *	Iron Oxide Ratio Std Dev	Concentration of Thorium Std Dev	
Local Elevation Mean *ˆ	**Clay Mineral Ratio Mean *ˆ**	**Concentration of Uranium Mean *ˆ**	**Ecological Vegetation Class (EVC) Majority ***
Local Elevation Std Dev ˆ	Clay Mineral Ratio Std Dev	Concentration of Uranium Std Dev	
Slope Mean *ˆ	Red Reflectance Mean	Aeromagnetic (Total Magnetic Intensity) Mean *ˆ	
Slope Std Dev *	Red Reflectance Std Dev	Aeromagnetic (Total Magnetic Intensity) Std Dev	
Surface Terrain Roughness Index Mean	Green Reflectance Mean	Aeromagnetic (first vertical derivative) Mean	
Surface Terrain Roughness Index Std Dev	Green Reflectance Std Dev	Aeromagnetic (first vertical derivative) Std Dev	
	Blue Reflectance Mean		
	Blue Reflectance Std Dev		

4. Results

In this study, 78.9% of known stony rises were detected, with an additional 2716 potential stony rises being identified (Figure 5). The RF model performance (e.g., the number of classified OBIA segments rather than whole stony rises) was assessed with the Kappa Coefficient, Out of Bag (OOB) error, as well as the 95% confidence level, precision and recall for each class (0 and 1). The Kappa Coefficient was 0.66 and the OOB error was 6.7%. For both classes, the 95% confidence interval was $\pm$0.97%. The precision for class 0 (non-stony rise segment) is 0.98, while class 1 (stony-rise segment) has 0.76. The recall for class 0 is 0.99, and 0.60 for class 1. There were 7531 false positive segments detected, and 16,032 false negative segments detected (Table 3).

Table 3. A confusion matrix detailing the prediction results of segments from the RF classification, where 0 is a non-stony rise segment and 1 is a stony rise segment.

	Reference	
Prediction	**0**	**1**
0	771,515	16,032
1	7531	23,966

The false positives of the potential new stony rises were manually inspected against high resolution aerial imagery, slope maps, and a DEM-derived hillshade. Of the detected false positives, 90.3% were associated with a potential new stony rise, 7.1% were associated with an existing stony rise, and the remaining 2.6% were associated with dams and dam infrastructure, roads and road infrastructure, grasslands, and quarries. No false positives occurred within the volcanic lakes. The false negatives were mainly found in the center ridgelines of stony rises and on the edges of stony rises with flatter slopes.

Figure 6 highlights the intricacy of the landscape across the study area and how stony rises were detected throughout. Figure 6a highlights the standalone and defined stony rises within the study area. Here, new stony rise sites have been identified (in green) independently of existing stony rises (in yellow and red). Figure 6b shows a cluster of newly detected stony rises (in green) in an area that hosts prominent and complex stony rises adjacent to a series of volcanic lakes, highlighting the success of the RF algorithm in rugged terrain. Figure 6c shows smaller and flatter stony rises, which are more concentrated in the southern portions of the study area. Figure 6d highlights standalone stony rises; however, these are flatter compared to some of their northern counterparts.

Table 4 highlights the variables of importance based on the mean decrease Gini coefficient, as well as comparing the ranking of the predictor variables used in Fraser et al. [8]. In this study, 12 variables were useful for mapping the stony rises of Warrion Hill and Red Rock. These variables are also shown in bold in Table 2. It was found that topographic variables were the most important as they consisted of 5 out of the 12 Gini variables of importance. The top performing variable was slope mean, whereas the least performing variable was the vegetation class majority. Some discussion about the performance of these variables in this study and in comparison, to Fraser et al. [8], are given in the following section.

Table 4. The variables of importance of the input predictor variables (left) compared to the ranking of predictor variables used in Fraser et al. [8] (right).

Predictor Variable	**Predictor Variable of Importance (by Mean Decrease Gini)**	**Predictor Variable Ranking from Fraser et al. [8]**
Slope Mean	5011	Local Elevation Mean
Local Elevation Mean	3070	Concentration Thorium Mean
Concentration of Potassium Mean	2345	Aeromagnetic (TMI) Mean
Normalized Difference Water Index (NDWI) Mean	2183	Concentration of Uranium Mean
Concentration Thorium Mean	1996	Clay Mineral Ratio Mean
DEM of Difference Mean	1918	Normalized Difference Water Index (NDWI) Mean
Slope Std Dev	1885	Slope Mean
Aeromagnetic (TMI) Mean	1738	Local Elevation Standard Deviation
Concentration of Uranium Mean	1737	
Clay Mineral Ratio Mean	1567	
DEM of Difference Std Dev	1480	
Vegetation Class Mean	364	

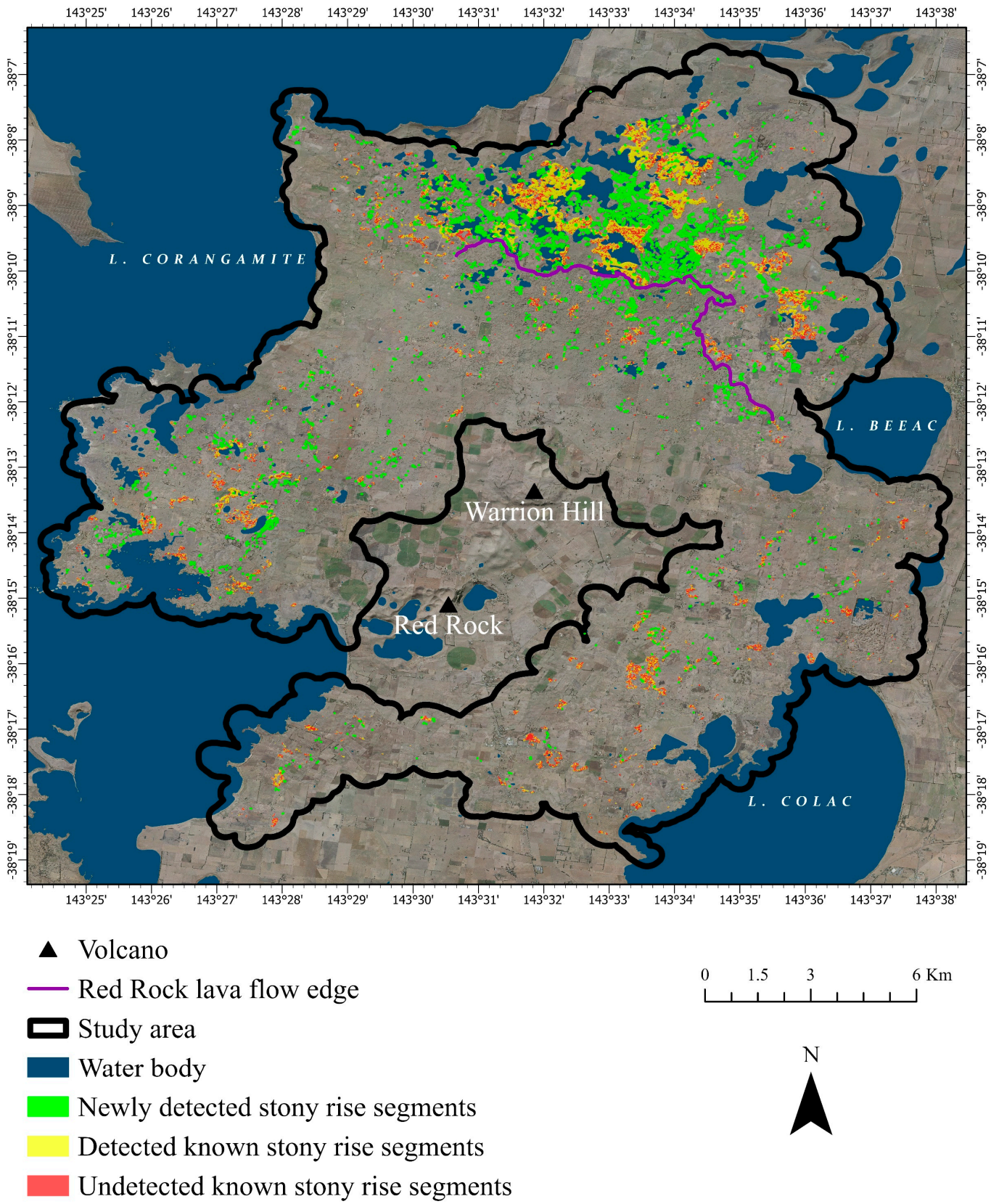


Figure 5. Predicted stony rises, where green shows the newly detected stony rise segments, yellow shows the detected known stony rise segments, and red is the undetected known stony rise segments. These are overlaid on a true color composite imagery and a DEM-derived hillshade. Additionally, the edge of the Red Rock lava has been mapped to highlight the changes in the volcanic landscape.

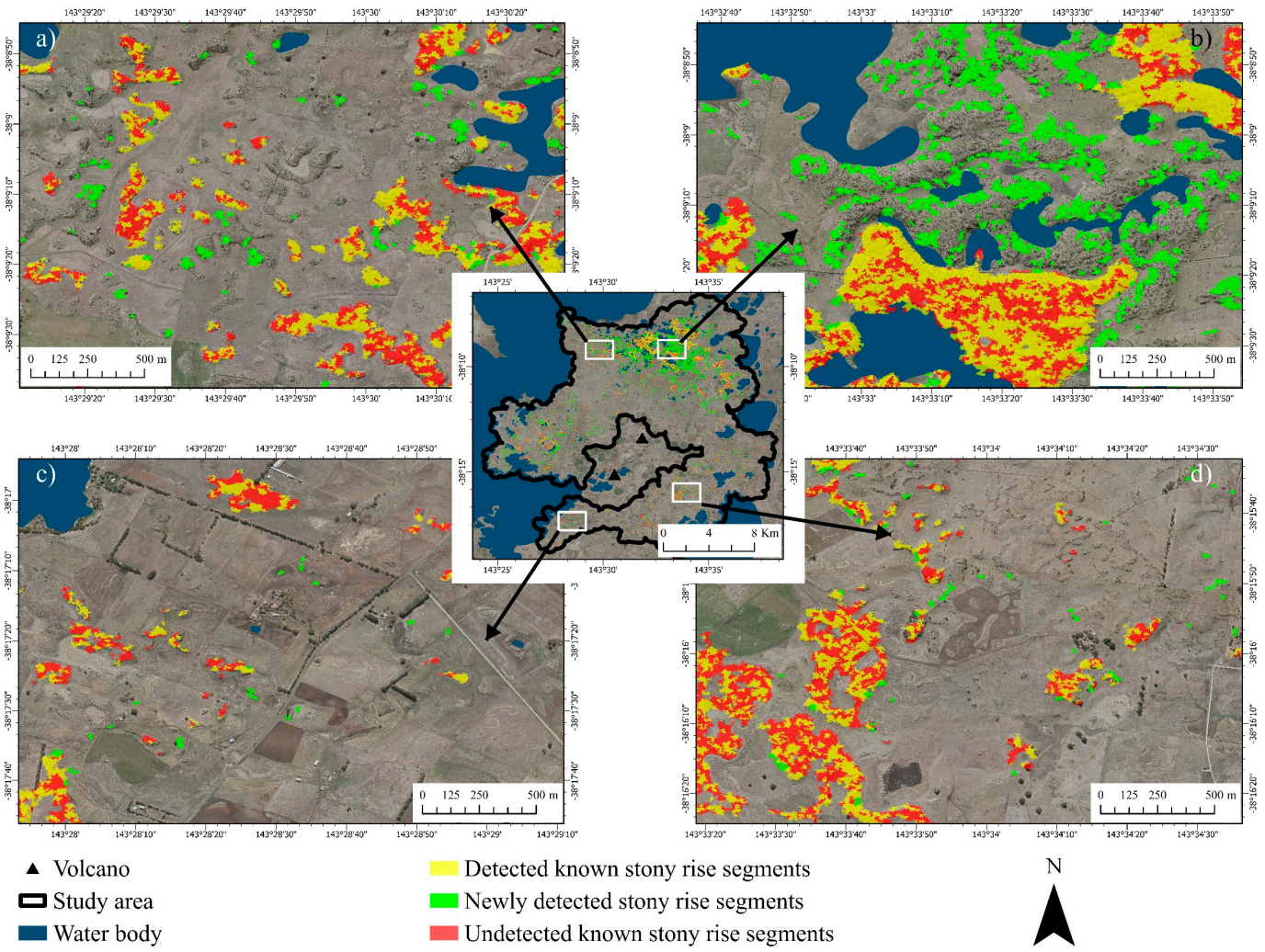


Figure 6. Subsections of the final output, highlighting the output of the Random Forest algorithm against the training data and the newly identified stony rise sites, which vary according to (**a**) clearly defined stony rises; (**b**) large and complex clusters of stony rises; (**c**) small and flatter stony rises in the landscape; (**d**) standalone and flat stony rises in the landscape. The stony rises are overlain on a true color composite imagery and a DEM-derived hillshade.

5. Discussion

This study aimed to map the stony rises across the geological unit of the Warrion Hill and Red Rock Volcanic Complex lava flows using remote sensing datasets and machine learning, as well as test the scalability and transferability of the methodology developed by Fraser et al. [8]. The following section presents and discusses important aspects of these results.

The methodology of an object-based RF approach was successful in detecting young stony rises (~42,000 years old) with an ensemble of predictor variables. In total, 78.9% of previously identified stony rises were detected, with an additional 2716 potential stony rises being detected. A number of important results are identified. Firstly, the newly detected stony rise segments are mainly concentrated in the northern parts of the study area, with a small clustering in the western portion of the study area. Since the terrain of the lava flows from Warrion Hill and Red Rock varies in topography, this has likely impacted the detection of stony rises. For instance, many of the false negatives are occurring on the center and edges of the stony rises. Since some stony rises have flat ridgelines and non-uniform slopes [10,17,18], there is potential for these flatter parts of the stony rise to be confused as

flat grasslands by the RF classification. Although new stony rises are being detected in the southern part of the study area, this is happening at a lower frequency. This is potentially due to the distribution of the training data and the topography of the stony rise being flatter and similar to that of the surrounding landscape. This has implications for data collection prior to the use of the approach presented here and discussed later.

Secondly, the Warrion Hill lava flows north of the volcano actually consist of two separate flows of different ages, with a younger flow in the south covering an older flow to the north (Figure 5). The stony rises on the northern flow are larger, taller, and have steeper slopes, whereas the surface of the southern flow is relatively smooth with few, if any, stony rises. This is probably related to a faster lava-supply rate for the younger flow, as previously discussed; it is unrelated to the relative age. One of the Red Rock cones was dated as 42,000 years old [13]; the northern flow from Red Rock is likely to be of this age based on the preservation of its stony rises, and the southern flow from Red Rock is even younger. Cas et al. [7] encouraged the combination of various datasets such as aerial and satellite imagery, LiDAR, and airborne geophysical data, to develop local detailed maps of lava flows and help establish a chronology of volcanic events and their spatial relationships to their volcanic landforms. The present study is a good example of this approach.

The location of the training data has had an influence on the detection of previously unknown stony rises. Given that the majority of stony rises in the study area are clustered in the northern portion of the study area, most of the training data is derived from here (608 stony rises). This resulted in an imbalance of training data where 282 stony rises (~15% of the training segments) are located in the southern portion of the study area. A consequence of this imbalance has resulted in fewer new stony rises being identified in the southern half. It has been suggested that when performing RF classifications, the best classification accuracy and certainty results are obtained when the training data distribution is balanced [65]. However, this may not always be possible when working a natural phenomenon such as landform distribution. The training data imbalance faced in this study may be the result of where stony rises are naturally distributed in the landscape, reflecting where the lava flowed from Warrion Hill and Red Rock.

Initially, the same stony rise threshold used in Fraser et al. [8] was applied to this study, where the only threshold that needed to be applied was stony rise purity, where $\geq$45% of an image object fell within a known stony rise polygon. However, it quickly became apparent that the stony rise purity threshold needed to be refined and a topography threshold, in the form of slope, needed to be added to reflect the complexity of the landscape. As a result of the complex topography of the younger stony rises within the study area, a purity threshold needed to be applied to the training data ($\geq$80% of a segment falling within a known stony rise polygon) and a minimum slope of 1.5° in this study. These thresholds greatly improved the quality of the training data while also greatly reducing the number of true false positives, where only 2.55% of false positives were not associated with an existing stony rise or a new stony rise site. This highlights the importance of having the correct training data parameters across differently aged landforms to help minimize the number of true false positives. The results of this study also highlight how the thresholds implemented affected the classification of known stony rises. Due to stony rises having flat ridgelines [10,17,18] and inconsistent slopes, some of the ridgelines and edges of known stony rises, particularly in the southern portion of the study area, have not been detected due to them not meeting the minimum slope requirement of 1.5°. This could help explain the high number of false negatives (16,062 segments) and why some stony rises missed detection.

As current trends in geomorphological landform detection are only beginning to incorporate multi-source data [8,27,59,66,67], it is important to ensure that the datasets

used are at an appropriate scale where the phenomenon can be mapped. In this study, the largest spatial resolution was 50 m, found in the airborne geophysical datasets. While this spatial resolution is too low to map individual stony rises, it is high enough where the generalization of the radiometric elements and geomagnetics can still have an impact on the detection of stony rises and the lava flow as a whole. Ideally, all datasets used in this study would be captured at the same time and have a spatial resolution of at least 5 m to detect smaller stony rises; however we are currently limited to the present technology and open-sourced data available. Fraser et al. [8] was able to acquire LiDAR data and aerial imagery that was captured at the same time, which may have aided in a higher stony rise detection accuracy. As governments capture higher spatial resolution LIDAR and aerial imagery across the VVP, this will provide more opportunities to study eruption sequencing for each volcanic complex [7]. Nonetheless, studies that are currently incorporating medium resolution datasets are achieving detection accuracies above 70% [8,27,66,67].

Another important component of this study was to determine the importance of predictor variables for mapping stony rises across different study areas using the technique of Fraser et al. [8]. It was found that the number of predictor variables and their importance can vary significantly when mapping stony rises of different ages. Specifically, this study found that extra predictor variables were required and that their ranking of importance differed.

For example, the 12 predictor variables used in this study included topographic (slope gradient, local elevation, and DEM of Difference (change in height)), spectral (NDWI and Clay Mineral Ratio), airborne geophysical (K, Th, U, and TMI), and vegetation information (EVC). This is contrary to Fraser et al. [8], where only eight predictor variables were used to map stony rises (slope mean, local elevation mean and standard deviation, concentration of Th and U mean, Total magnetic intensity mean, NDWI mean, and the Clay mineral Index mean). The common predictor variables to Fraser et al. [8] include slope mean, local elevation mean, concentration of Th and U mean, Aeromagnetic (TMI) mean, NDWI mean, and the Clay Mineral Ratio mean. The top three variables in this study are slope mean, local elevation mean, and concentration of Potassium mean, whereas Fraser et al. [8] found the top three to be local elevation mean, concentration of Thorium mean, and Aeromagnetic (TMI) mean. These differences are believed to be the result of the different ages of the stony rises.

The younger age of the lava flow in this study area is likely a factor in the ability to map stony rises using the technique of Fraser et al. [8]. The Mt Fraser stony rises mapped in Fraser et al. [8] are much older (~800,000 years old) than the younger lava flows from the Warrion Hill and Red Rock volcanoes. The results from this study suggest that topographic variables are more important to characterize and map younger stony rises (~42,000 years old) as five topographic variables were needed to successfully map stony rises compared to the three used for the Mt Fraser lava flow [8]. Stony rises found on lava flows younger than 50,000 years old are well preserved and resemble their original size due to the lack of weathering [8,12,13], whereas stony rises on lava flows that are >500,000 years old are flatter due to severe weathering and have well developed clay soils [8]. Older stony rises, as a result, appear to rely more on geophysical and spectral information for successful detection and mapping [8]. This is reflected in the slope mean predictor variable, where in Fraser et al. [8], slope mean was the seventh best performing predictor variable, compared to this study where slope mean was the top performing predictor variable. This is due to the topographic complexity of the stony rises from the Warrion Hill/Red Rock lava flows, which are more rugged, consisting of steep slopes and being significantly elevated from the surrounding grasslands. These important and complex topographic characteristics needed

to be reflected in the predictor variables chosen for the RF classification, resulting in five topographic predictor variables used for mapping younger stony rises.

In addition, the Potassium (K), Thorium (Th), and Uranium (U) content in the lava of stony rises appears to be an important factor. Within the geophysical variables used in this study, K mean was found to be the most important, followed by Th mean and U mean. Younger basalt lava flows have higher concentrations of K, but as they age, K decays faster, revealing the concentrations of Th and U [7,68]. If similarly aged stony rises were to be mapped (e.g., the Mt Eccles and Mt Napier lava flows), the concentration of K would most likely be a high performing predictor variable compared to other geophysical variables. Additionally, when mapping older stony rises, such as the ones from the Mt Fraser lava flow (~800,000 years old), it was found that K had decayed too much for it to be considered a predictor variable [8]. This suggests that the age of stony rises being mapped influences the choice of the geophysical predictor variables needed for successful landform detection.

The importance of vegetation related variables when mapping stony rises of different ages was also noticed. In this study area, vegetation played a more important role in mapping the younger stony rises. This was at first surprising, as vegetation was not used as a predictor variable to map the older stony rises (~800,000 years old) from the Mt Fraser lava flow [8]. When looking closely at the vegetation class distribution across the Warrion Hill/Red Rock lava flows, there is a clear divide between the northern and southern portions of the study area, following the topographical irregularities found in the landscape. In the north, where the terrain is more rugged, Stony Rise Woodland is the dominant vegetation class, whereas the southern part of the study area has terrain that is flatter and undulating, hosting the dominant EVC of Plains Grassy Woodland. It was noted that when the EVC class majority was not added into the RF classification, the Kappa coefficient was not as high, meaning the classification output was more unreliable. This suggests that including contextual information of the landscape such as vegetation class and its distribution can influence stony rise classification at a landscape scale.

The present study is an example of how a ML methodology can be transferred and scaled to map a phenomenon that is found across different study sites. It has been suggested that the scalability of a ML methodology for landform mapping is useful for land planning purposes as this can provide insights into the evolution of complex physical landscapes [69]. While this study has shown this can be successfully done, the methodology needed to be adjusted to accommodate the data availability and landform differences across the study areas. The results of this study have some important implications to data collection if the machine learning technique of Fraser et al. [8] is to be applied to different study areas. Perhaps the most significantly different aspect of this study in comparison to Fraser et al. [8] is the lack of ground-based mapping of stony rises from the Warrion Hill/Red Rock lava flows. As a result, the training data was created using manual interpretation from slope maps and hillshaded DEMs after conducting field work to observe the stony rises and the landscape in person. With the stony rises in the study area being young (~42,000 years old) [13], the landscape is less weathered and therefore some of the stony rises are complex and difficult to interpret from the general lava flow. While this may have introduced some bias when creating the training data, it is recognized that landform mapping can be a subjective process when manual interpretation is involved [70]. Additionally, the repeatability of ML methodologies combined with remote sensing data such as LiDAR, means landforms can be detected objectively across different scales, and allows for landscape and landform recovery when dealing with historical datasets [69,71].

6. Conclusions

This study contributes to the mapping of stony rises across the Victorian Volcanic Plain (VVP), which are recognized as important landforms for geological, ecological, and cultural purposes [7,19,72,73]. Stony rises were detected to an accuracy of 78.9% using an object-based machine learning approach and a variety of topographic, spectral, geophysical, and vegetation predictor variables. This approach highlights that the optimal predictor variables needed are slope gradient, local elevation, and DEM of Difference (change in height), Normalized Difference Water Index (NDWI), Clay Mineral Ratio, the concentration of radiometric elements (K, Th, U), Total Magnetic Intensity (TMI), and Ecological Vegetation Class to map young stony rises (~42,000 years old) from an entire lava flow. Detailed maps created of such landforms allow for targeted geological, ecological, and cultural studies and analysis to occur in the form of field surveys. Additionally, this study highlights the unique nature of stony rises and how it takes a variety of predictor variables to map them across different ages.

Currently the mapping of stony rises is performed on a case-study scale, and this study highlights the transferability and scalability of using an ensemble of predictor variables and machine learning to map a whole geological unit of relatively young stony rises to an accuracy of 78.9%. This approach helps standardize a methodology towards mapping stony rises of different ages across the VVP, and could be applied to other young lava flows such as the Mt Eccles (~36.9 ka) [12] and Mt Napier (~48.5 ka) [13] lava flows, or on similar volcanic landforms (tumuli and lava rises) found worldwide [2–4].

Overall, this study was able to successfully map stony rises using an established methodology, highlighting that the predictor variables, thresholds, and training data and data availability may need to be altered and tailored to the landscape to produce a successful result when mapping recurring landforms across different study areas.

Author Contributions: Conceptualization, S.F., M.S.-B., L.H. and S.J.; methodology, S.F., M.S.-B., L.H. and S.J.; software, S.F.; validation, S.F., M.S.-B., L.H., J.W. and S.J.; formal analysis, S.F.; investigation, S.F.; resources, S.F.; data curation, S.F.; writing—original draft preparation, S.F., M.S.-B., L.H., J.W. and S.J.; writing—review and editing, S.F., M.S.-B., L.H., J.W. and S.J.; visualization, S.F.; supervision, M.S.-B., L.H. and S.J.; project administration, S.F., M.S.-B., L.H. and S.J.; funding acquisition, M.S.-B., L.H. and S.J. All authors have read and agreed to the published version of the manuscript.

Funding: This research was funded by RMIT University Science Scholarship.

Data Availability Statement: All remotely sensed datasets used have been obtained from open-sourced repositories and have been cited as such throughout the paper.

Acknowledgments: We recognize the importance of stony rises for Aboriginal Australians and acknowledge the Eastern Maar Aboriginal Corporation as the traditional owners of the land in which this study takes place. We thank RMIT University Science Scholarship for funding this research and the various data custodians who provide open-source data. We would also like to thank Robert Hewson and Trung Nguyen for their support at various stages of this study. We would like to thank the anonymous reviewers for their suggestions which have improved the quality of this paper.

Conflicts of Interest: The authors declare no conflicts of interest.

References

1. Boyce, J. The Newer Volcanics Province of Southeastern Australia: A New Classification Scheme and Distribution Map for Eruption Centres. *Aust. J. Earth Sci.* **2013**, *60*, 449–462. [CrossRef]
2. Walker, G.P.L. Structure, and Origin by Injection of Lava under Surface Crust, of Tumuli, "Lava Rises", "Lava-Rise Pits", and "Lava-Inflation Clefts" in Hawaii. *Bull. Volcanol.* **1991**, *53*, 546–558. [CrossRef]
3. Wentworth, C.K.; Macdonald, G.A. Structures and Forms of Basaltic Rocks in Hawaii. In *Geological Survey Bulletin*; United States Government Publishing Office: Washington, DC, USA, 1953.

4. Skeats, E.W.; James, A.V.G. Basaltic Barriers and Other Surface Features of the Newer Basalts of Western Victoria. *Proc. R. Soc. Vic.* **1937**, *49*, 245–278.
5. Heath, M.; Phillips, D.; Matchan, E.L. Basalt Lava Flows of the Intraplate Newer Volcanic Province in South-East Australia (Melbourne Region): 40Ar/39Ar Geochronology Reveals ~8 Ma of Episodic Activity. *J. Volcanol. Geotherm. Res.* **2020**, *389*, 106730. [CrossRef]
6. Smith, B.W.; Prescott, J.R. Thermoluminescence Dating of the Eruption at Mt Schank, South Australia. *Aust. J. Earth Sci.* **1987**, *34*, 335–342. [CrossRef]
7. Cas, R.A.F.; van Otterloo, J.; Blaikie, T.N.; van den Hove, J. The Dynamics of a Very Large Intra-Plate Continental Basaltic Volcanic Province, the Newer Volcanics Province, SE Australia, and Implications for Other Provinces. *Geol. Soc. Spec. Publ.* **2017**, *446*, 123–172. [CrossRef]
8. Fraser, S.; Soto-Berelov, M.; Holden, L.; Hewson, R.; Webb, J.; Jones, S. Mapping Stony Rise Landforms Using a Novel Remote Sensing, Geophysical, and Machine Learning Approach. *Geomorphology* **2024**, *450*, 109070. [CrossRef]
9. Joyce, E.B. *A New Regolith Landform Map of the Western Victorian Volcanic Plains, Victoria, Australia*; Taylor, G., Pain, C., Eds.; Regolith: Kalgoorlie, WA, Australia, 1998; pp. 117–126.
10. Moloney, D. *City of Whittlesea: Stage Two Dry Stone Wall Study: Thematic History and Precincts*; City of Whittlesea: South Morang, VIC, Australia, 2020.
11. Heath, M.; Phillips, D.; Matchan, E.L. An Evidence-Based Approach to Accurate Interpretation of 40Ar/39Ar Ages from Basaltic Rocks. *Earth Planet. Sci. Lett.* **2018**, *498*, 65–76. [CrossRef]
12. Matchan, E.L.; Phillips, D.; Jourdan, F.; Oostingh, K. Early Human Occupation of Southeastern Australia: New Insights from 40Ar/39Ar Dating of Young Volcanoes. *Geology* **2020**, *48*, 390–394. [CrossRef]
13. Oostingh, K.F.; Jourdan, F.; Matchan, E.L.; Phillips, D. 40Ar/39Ar Geochronology Reveals Rapid Change from Plume-Assisted to Stress-Dependent Volcanism in the Newer Volcanic Province, SE Australia. *Geochem. Geophys. Geosyst.* **2017**, *18*, 1065–1089. [CrossRef]
14. Ollier, C.D. Landforms of the Newer Volcanic Province of Victoria. In *Landform Studies from Australia and New Guinea*; Jennings, J.N., Mabbutt, J.A., Eds.; Australian National University Press: Canberra, NSW, Australia, 1967; pp. 315–340.
15. Department of Planning and Community Development. *South West Victoria Landscape Assessment Study: Significant Landscapes*; Department of Planning and Community Development: Melbourne, VIC, Australia, 2013.
16. McNiven, I. Aboriginal Settlement of the Saline Lake and Volcanic Landscapes of Corangamite Basin, Western Victoria. *Artefact* **1998**, *21*, 63–94.
17. Orr, A. *Precinct Structure Plan 1067 Donnybrook Aboriginal Heritage Impact Assessment*; Terra Culture: Northcote, VIC, Australia, 2013.
18. Clarke, A. *Lake Condah Project Aboriginal Archaeology: Resource Inventory*; Aboriginal Affairs Victoria: Melbourne, VIC, Australia, 1991.
19. Clarke, A. Romancing the Stones. The Cultural Construction of an Archaeological Landscape in the Western District of Victoria. *Archaeol. Ocean.* **1994**, *29*, 1–15. [CrossRef]
20. Coutts, P.J.F.; Frank, R.K.; Hughes, P.; Vanderwal, R.L. *Aboriginal Engineers of the Western District, Victoria*; Aboriginal Affairs Victoria: Melbourne, VIC, Australia, 1978.
21. Tulloch, J. *An Archaeological Survey of 1910 Donnybrook Road, Yan Yean, Victoria*; Biosis Research: Melbourne, VIC, Australia, 2001.
22. Van Waarden, R.; Simmons, S. *Lake Condah: Review and Assessment*; Victoria Archaeological Survey: Mitcham, VIC, Australia, 1992.
23. Jasiewicz, J.; Stepinski, T.F. Geomorphons-a Pattern Recognition Approach to Classification and Mapping of Landforms. *Geomorphology* **2013**, *182*, 147–156. [CrossRef]
24. Cody, T.R.; Anderson, S.L. LiDAR Predictive Modeling of Pacific Northwest Mound Sites: A Study of Willamette Valley Kalapuya Mounds, Oregon (USA). *J. Archaeol. Sci. Rep.* **2021**, *38*, 103008. [CrossRef]
25. Feizizadeh, B.; Kazemi Garajeh, M.; Blaschke, T.; Lakes, T. An Object Based Image Analysis Applied for Volcanic and Glacial Landforms Mapping in Sahand Mountain, Iran. *Catena* **2021**, *198*, 105073. [CrossRef]
26. Freeland, T.; Heung, B.; Burley, D.V.; Clark, G.; Knudby, A. Automated Feature Extraction for Prospection and Analysis of Monumental Earthworks from Aerial LiDAR in the Kingdom of Tonga. *J. Archaeol. Sci.* **2016**, *69*, 64–74. [CrossRef]
27. Kazemi Garajeh, M.; Feizizadeh, B.; Weng, Q.; Rezaei Moghaddam, M.H.; Kazemi Garajeh, A. Desert Landform Detection and Mapping Using a Semi-Automated Object-Based Image Analysis Approach. *J. Arid Environ.* **2022**, *199*, 104721. [CrossRef]
28. Mitkari, K.V.; Arora, M.K.; Tiwari, R.K.; Sofat, S.; Gusain, H.S.; Tiwari, S.P. Large-Scale Debris Cover Glacier Mapping Using Multisource Object-Based Image Analysis Approach. *Remote Sens.* **2022**, *14*, 3202. [CrossRef]
29. Pedersen, G.B.M. Semi-Automatic Classification of Glaciovolcanic Landforms: An Object-Based Mapping Approach Based on Geomorphometry. *J. Volcanol. Geotherm. Res.* **2016**, *311*, 29–40. [CrossRef]
30. Verhagen, P.; Drâguţ, L. Object-Based Landform Delineation and Classification from DEMs for Archaeological Predictive Mapping. *J. Archaeol. Sci.* **2012**, *39*, 698–703. [CrossRef]

31. Guyot, A.; Hubert-Moy, L.; Lorho, T. Detecting Neolithic Burial Mounds from LiDAR-Derived Elevation Data Using a Multi-Scale Approach and Machine Learning Techniques. *Remote Sens.* **2018**, *10*, 225. [CrossRef]
32. Orengo, H.A.; Conesa, F.C.; Garcia-Molsosa, A.; Lobo, A.; Green, A.S.; Madella, M.; Petrie, C.A. Automated Detection of Archaeological Mounds Using Machine-Learning Classification of Multisensor and Multitemporal Satellite Data. *Proc. Natl. Acad. Sci. USA* **2020**, *117*, 18240–18250. [CrossRef] [PubMed]
33. Siqueira, R.G.; Veloso, G.V.; Fernandes-Filho, E.I.; Francelino, M.R.; Schaefer, C.E.G.R.; Corrêa, G.R. Evaluation of Machine Learning Algorithms to Classify and Map Landforms in Antarctica. *Earth Surf. Process. Landf.* **2022**, *47*, 367–382. [CrossRef]
34. Stott, D.; Kristiansen, S.M.; Sindbæk, S.M. Searching for Viking Age Fortresses with Automatic Landscape Classification and Feature Detection. *Remote Sens.* **2019**, *11*, 1881. [CrossRef]
35. Zhao, W.-F.; Xiong, L.-Y.; Ding, H.; Tang, G.-A. Automatic Recognition of Loess Landforms Using Random Forest Method. *J. Mt. Sci.* **2017**, *14*, 885–897. [CrossRef]
36. Juel, A.; Groom, G.B.; Svenning, J.C.; Ejrnæs, R. Spatial Application of Random Forest Models for Fine-Scale Coastal Vegetation Classification Using Object Based Analysis of Aerial Orthophoto and DEM Data. *Int. J. Appl. Earth Obs. Geoinf.* **2015**, *42*, 106–114. [CrossRef]
37. Silveira, E.M.O.; Silva, S.H.G.; Acerbi-Junior, F.W.; Carvalho, M.C.; Carvalho, L.M.T.; Scolforo, J.R.S.; Wulder, M.A. Object-Based Random Forest Modelling of Aboveground Forest Biomass Outperforms a Pixel-Based Approach in a Heterogeneous and Mountain Tropical Environment. *Int. J. Appl. Earth Obs. Geoinf.* **2019**, *78*, 175–188. [CrossRef]
38. De Castro, A.I.; Torres-Sánchez, J.; Peña, J.M.; Jiménez-Brenes, F.M.; Csillik, O.; López-Granados, F. An Automatic Random Forest-OBIA Algorithm for Early Weed Mapping between and within Crop Rows Using UAV Imagery. *Remote Sens.* **2018**, *10*, 285. [CrossRef]
39. Lebourgeois, V.; Dupuy, S.; Vintrou, É.; Ameline, M.; Butler, S.; Bégué, A. A Combined Random Forest and OBIA Classification Scheme for Mapping Smallholder Agriculture at Different Nomenclature Levels Using Multisource Data (Simulated Sentinel-2 Time Series, VHRS and DEM). *Remote Sens.* **2017**, *9*, 259. [CrossRef]
40. Li, M.; Ma, L.; Blaschke, T.; Cheng, L.; Tiede, D. A Systematic Comparison of Different Object-Based Classification Techniques Using High Spatial Resolution Imagery in Agricultural Environments. *Int. J. Appl. Earth Obs. Geoinf.* **2016**, *49*, 87–98. [CrossRef]
41. Vogels, M.F.A.; de Jong, S.M.; Sterk, G.; Addink, E.A. Agricultural Cropland Mapping Using Black-and-White Aerial Photography, Object-Based Image Analysis and Random Forests. *Int. J. Appl. Earth Obs. Geoinf.* **2017**, *54*, 114–123. [CrossRef]
42. Fallatah, A.; Jones, S.; Mitchell, D. Object-Based Random Forest Classification for Informal Settlements Identification in the Middle East: Jeddah a Case Study. *Int. J. Remote Sens.* **2020**, *41*, 4421–4445. [CrossRef]
43. Amini, S.; Homayouni, S.; Safari, A.; Darvishsefat, A.A. Object-Based Classification of Hyperspectral Data Using Random Forest Algorithm. *Geo-Spat. Inf. Sci.* **2018**, *21*, 127–138. [CrossRef]
44. Nasiri, V.; Hawryło, P.; Janiec, P.; Socha, J. Comparing Object-Based and Pixel-Based Machine Learning Models for Tree-Cutting Detection with PlanetScope Satellite Images: Exploring Model Generalization. *Int. J. Appl. Earth Obs. Geoinf.* **2023**, *125*, 103555. [CrossRef]
45. Ding, H.; Na, J.; Jiang, S.; Zhu, J.; Liu, K.; Fu, Y.; Li, F. Evaluation of Three Different Machine Learning Methods for Object-Based Artificial Terrace Mapping—A Case Study of the Loess Plateau, China. *Remote Sens.* **2021**, *13*, 1021. [CrossRef]
46. Breiman, L. Random Forests. *Mach. Learn.* **2001**, *45*, 5–32. [CrossRef]
47. Rodriguez-Galiano, V.F.; Ghimire, B.; Rogan, J.; Chica-Olmo, M.; Rigol-Sanchez, J.P. An Assessment of the Effectiveness of a Random Forest Classifier for Land-Cover Classification. *ISPRS J. Photogramm. Remote Sens.* **2012**, *67*, 93–104. [CrossRef]
48. Bureau of Meteorology; CSIRO. *Corangamite Region at a Glance A Climate Guide for Agriculture Corangamite, Victoria*; Bureau of Meteorology: Melbourne, VIC, Australia, 2019.
49. Blaikie, T.; Piganis, F.; Cas, R.; Ailleres, L.; Betts, P. The Red Rock Volcanic Complex. In *Proceedings of the VF01: Factors That Influence Varying Eruption Styles (From Magmatic to Phreato-Magmatic) in Intraplate Continental Basaltic Volcanic Provinces: The Newer Volcanics Province of South-Eastern Australia*; Cas, R., Blaikie, T., Boyce, J., Hayman, P., Jordan, S., Piganis, F., Prata, G., van Otterloo, J., Eds.; The Nomadic Explorers: Melbourne, VIC, Australia, 2011.
50. Hon, K.; Kauahikaua, J.; Denlinger, R.; Mackay, K. Emplacement and Inflation of Pahoehoe Sheet Flows: Observations and Measurements of Active Lava Flows on Kilauea Volcano, Hawaii. *Geol. Soc. Am. Bull.* **1994**, *106*, 351–370. [CrossRef]
51. Fraser, S.; Soto-Berelov, M.; Holden, L.; Jones, S. Identifying Metrics for the Spatial Characterisation of Stony Rise Landforms across the Landscape. In *Proceedings of the Excavations, Surveys and Heritage Management in Victoria*; Kelly, D., Frankel, D., Foley, E., Lawrence, S., Spry, C., Eds.; La Trobe University: Melbourne, VIC, Australia, 2022; Volume 11, pp. 15–28.
52. Department of Environment Land Water and Planning. 2006-07 South-West Region LiDAR—Corangamite. 2016.
53. Copernicus S2B_MSIL2A_20211101T002059_N0301_R116_T54HYC_20211101T021017.SAFE 2021. Available online: https://dataspace.copernicus.eu/ (accessed on 22 November 2023).
54. Gao, B.C. NDWI—A Normalized Difference Water Index for Remote Sensing of Vegetation Liquid Water from Space. *Remote Sens. Environ.* **1996**, *58*, 257–266. [CrossRef]

55. Pour, A.B.; Ranjbar, H.; Sekandari, M.; Abd El-Wahed, M.; Hossain, M.S.; Hashim, M.; Yousefi, M.; Zoheir, B.; Wambo, J.D.T.; Muslim, A.M. Remote Sensing for Mineral Exploration. In *Geospatial Analysis Applied to Mineral Exploration: Remote Sensing, GIS, Geochemical, and Geophysical Applications to Mineral Resources*; Elsevier: Amsterdam, The Netherlands, 2023; pp. 17–149. [CrossRef]
56. Department of Environment Land Water and Planning. 2018–2019 South West Rural Photography. 2019.
57. Department of Primary Industries. Victoria—Gridded Airborne Geophysical Data, and Located and Gridded Gravity 2008. Available online: https://earthresources.efirst.com.au/product.asp?pID=22&cID=13 (accessed on 19 October 2022).
58. Department of Environment Land Water and Planning Native Vegetation—Modelled 1750 Ecological Vegetation Classes 2022. Available online: https://www.data.vic.gov.au/ (accessed on 1 August 2022).
59. Rocamora, I.; Ienco, D.; Ferry, M. Multi-Source Deep-Learning Approach for Automatic Geomorphological Mapping: The Case of Glacial Moraines. *Geo-Spat. Inf. Sci.* **2024**, *27*, 1747–1766. [CrossRef]
60. Orfeo ToolBox Orfeo ToolBox. Available online: https://www.orfeo-toolbox.org/about-otb/ (accessed on 5 January 2023).
61. Boukir, S.; Jones, S.; Reinke, K. Fast Mean-Shift Based Classification of Very High Resolution Images: Application to Forest Cover Mapping. *ISPRS Ann. Photogramm. Remote Sens. Spat. Inf. Sci.* **2012**, *1*, 111–116. [CrossRef]
62. Anders, N.S.; Seijmonsbergen, A.C.; Bouten, W. Segmentation Optimization and Stratified Object-Based Analysis for Semi-Automated Geomorphological Mapping. *Remote Sens. Environ.* **2011**, *115*, 2976–2985. [CrossRef]
63. Ma, W.; Ye, X.; Tu, F.; Hu, F. Carat: An R Package for Covariate-Adaptive Randomization in Clinical Trials. *J. Stat. Softw.* **2023**, *107*, 1–27. [CrossRef]
64. Liaw, A.; Wiener, M. Classification and Regression by RandomForest. *R News* **2002**, *2*, 18–22.
65. Mellor, A.; Boukir, S.; Haywood, A.; Jones, S. Exploring Issues of Training Data Imbalance and Mislabelling on Random Forest Performance for Large Area Land Cover Classification Using the Ensemble Margin. *ISPRS J. Photogramm. Remote Sens.* **2015**, *105*, 155–168. [CrossRef]
66. Li, S.; Xiong, L.; Tang, G.; Strobl, J. Deep Learning-Based Approach for Landform Classification from Integrated Data Sources of Digital Elevation Model and Imagery. *Geomorphology* **2020**, *354*, 107045. [CrossRef]
67. Veronesi, F.; Hurni, L. Random Forest with Semantic Tie Points for Classifying Landforms and Creating Rigorous Shaded Relief Representations. *Geomorphology* **2014**, *224*, 152–160. [CrossRef]
68. Dickson, L.; Scott, K.M. Interpretation of Aerial Gamma-Ray Surveys-Adding the Geochemical Factors. *AGSO J. Aust. Geol. Geophys.* **1997**, *17*, 187–200.
69. Cignetti, M.; Godone, D.; Ferrari Trecate, D.; Baldo, M. New Paradigms for Geomorphological Mapping: A Multi-Source Approach for Landscape Characterization. *Remote Sens.* **2025**, *17*, 581. [CrossRef]
70. Smith, M.J.; Wise, S.M. Problems of Bias in Mapping Linear Landforms from Satellite Imagery. *Int. J. Appl. Earth Obs. Geoinf.* **2007**, *9*, 65–78. [CrossRef]
71. Sevara, C.; Verhoeven, G.; Doneus, M.; Draganits, E. Surfaces from the Visual Past: Recovering High-Resolution Terrain Data from Historic Aerial Imagery for Multitemporal Landscape Analysis. *J. Archaeol. Method Theory* **2018**, *25*, 611–642. [CrossRef] [PubMed]
72. Goldfarb, A.; Spry, C.; Jones, R.; Wandin, A.; Mullins, B.; Stephenson-Gordon, G.; Stephenson, B.; Flatley, A.; Kurpiel, R.; Bruce, A.; et al. A Tale as Old as Time: Stony Rises on Wurundjeri Woi-Wurrung Country, South-Eastern Australia. In *Proceedings of the 2023 Excavations, Surveys and Heritage Management in Victoria*; Kelly, D., Frankel, D., Foley, E., Lawrence, S., Spry, C., Berelov, I., Canning, S., Eccleston, M., Eds.; La Trobe: Melbounre, VIC, Australia, 2023; Volume 12, pp. 19–32.
73. Mcconachie, F.; Mcalister, R. Mapping Cultural Values: A Case Study from Kalkallo, Melbourne Metropolitan Area. In *Proceedings of the Excavations, Surveys and Heritage Management in Victoria*; La Trobe: Melbourne, VIC, Australia, 2018; Volume 7, pp. 25–32.

Disclaimer/Publisher's Note: The statements, opinions and data contained in all publications are solely those of the individual author(s) and contributor(s) and not of MDPI and/or the editor(s). MDPI and/or the editor(s) disclaim responsibility for any injury to people or property resulting from any ideas, methods, instructions or products referred to in the content.